Effect of Plasma Sheaths on Earth Re-entry MHD Processes

Bernard Parent*, Prasanna T. Rajendran†
University of Arizona, Tucson, AZ 85721
and
Robert W. Moses‡, Christopher O. Johnston§, F. McNeil Cheatwood¶
NASA Langley Research Center, Hampton, VA 23681
and
Sergey O. Macheret‖
Purdue University, West Lafayette, IN 47907
and
Justin Little**
University of Washington, Seattle, WA 98195

The first study of the full coupling between the aerothermodynamics, the magnetohydrodynamics, and the plasma sheaths within earth entry flows is here performed. The problem tackled herein is representative of a force-generating MHD patch located between the plenum and the frustum of a capsule entering the earth's atmosphere at Mach 34. The reactions are obtained from a modified 11-species Park chemical solver. The physical model fully couples the drift-diffusion model for the sheaths to the multispecies Navier-Stokes equations for the plasma flow. The Hall and ion slip effects are taken into consideration within the plasma flow and within the sheaths. Results obtained indicate that the cathode sheath can exert significant resistance to current flow and thus reduce the MHD-generated force by 40% or more. The effect of the sheath on the MHD force is found to be more pronounced at lower applied magnetic field.

*Associate Professor, Aerospace and Mechanical Engineering, Member AIAA, bparent@arizona.edu
†Graduate Student, Aerospace and Mechanical Engineering
‡Aerospace Engineer, Atmospheric Flight and Entry Systems Branch
§Aerospace Engineer
¶Aerospace Engineer
‖Professor, School of Aeronautics and Astronautics
**Assistant Professor, Dept. of Aeronautics and Astronautics

I. Introduction

VARIOUS technologies based on the principles of magnetohydrodynamics (MHD) are under consideration to overcome the various challenges that are characteristic of planetary entry at high Mach number. One example is aerobraking in which the Lorentz force acting on the flow helps in slowing down the capsule when the atmosphere is not sufficiently dense to create enough pressure drag [1, 2, 3]. Another, called regenerative aerobraking, is using the Lorentz force not only to slow down the vehicle but also to generate power to recharge batteries or power on-board equipment [4, 5, 6]. Yet another MHD technology envisaged for planetary entry is the mitigation of the surface heat fluxes through increasing the shock standoff distance with the use of a magnetic field [7, 8, 9, 10]. Although the MHD technologies for planetary entry show great promise and have received considerable attention through various experimental and numerical studies, various physical phenomena taking place when a magnetic field interacts with an ionized gas at high speeds are still not well understood.

One such physical phenomenon that has received little attention to date is the plasma sheath. The sheath is a thin region separating the surfaces of the vehicle and the quasi-neutral plasma bulk and that is always significantly non-neutral. Although the sheath thickness may be only one tenth of the one of the boundary layer, the sheath can have a large impact on the amount of current that flows from electrode to electrode in a MHD system. This is due to the sheath near the cathode being characterized by a ion density several orders of magnitude higher than the electron density. Thus, the current within the cathode sheath is mostly ionic and not electronic as in the bulk of the plasma. Because the ions have a conductivity orders of magnitude less than the one of the electrons, this leads to a large resistance to current flow. In turn, because the Lorentz forces scale with the cross product of the current density and the magnetic field vectors, a reduction of the current leads to reduced MHD forces.

If the plasma sheaths are well known to affect current, why weren't they included in past simulations of planetary entry MHD? Solving the sheaths by themselves independently of the quasi-neutral bulk is not a problem. Although the wave speeds within the sheaths are high (typically hundreds of thousands of meters per second) and limit the integration time step to less than one nanosecond, this is not problematic because sheaths require only a few hundred nanoseconds to reach convergence. Thus, simulating sheaths on their own is not an issue and very fast convergence can be obtained in a few thousand iterations. The problem arises when trying to integrate the sheaths coupled to quasi-neutral regions of substantial size which require 1 millisecond or more to reach steady-state. Because the sheaths prevent an integration time step of more than one nanosecond or so to be used, millions of iterations or more are needed to reach convergence. Such leads to very poor computational efficiency because, for such a large number of iterations, one is forced to use very coarse meshes to keep the computational effort reasonable. Of course, the use of too coarse meshes leads to numerical error that is so excessive that the numerical results are not good approximations to the physical model. Perhaps for this reason, all previous simulations of planetary entry flows with MHD have neglected the effect of the plasma sheaths.

New numerical methods that were developed in the last decade shed hope that this barrier can be overcome. In Refs. [11, 12, 13, 14, 15], a new recast of the drift-diffusion plasma sheath model was shown to overcome the stiffness of the system and to permit much larger time steps to be used. Such recast is done without modifying the drift-diffusion physical model and is thus strictly a convergence acceleration method. Using this newly recast drift-diffusion model, it was possible

to integrate for the first time the plasma sheaths in fully-coupled form with the plasma flowing around a hypersonic re-entry vehicle in [16].

In this paper, we will use the recast drift-diffusion model applicable to a plasma in the presence of a magnetic field outlined in [15] to simulate for the first time the full coupling between the sheaths, the MHD process, and the fluid flow around a planetary entry capsule. The simulations are representative of the flow around a capsule re-entering the Earth at a Mach number of 34. The effect of the plasma sheaths on the MHD induced forces and heating is assessed.

II. Physical Model

The physical model consists of the drift-diffusion model coupled to the Navier-Stokes equations, electron energy transport equation, and total energy transport equation. We now outline all equations that make up the physical model solved in this study.

A. Drift-Diffusion Model

The mass conservation equation for each charged species can be expressed as a function of the kth charged species velocity $\boldsymbol{V}^k$ which includes both drift and diffusion, as follows:

$$\frac{\partial}{\partial t}\rho_k + \sum_i \frac{\partial}{\partial x_i}\rho_k \boldsymbol{V}_i^k = W_k \tag{1}$$

In the latter, ρ refers to the density (i.e., mass per unit volume) and the super/subscript k refers to the kth species which can be either electrons or ions. The chemical source term W_k corresponds to the net mass rate of creation of the kth species per unit volume due to chemical reactions, with all the reactions listed in Table 1. Also, $\boldsymbol{V}^k$ is the velocity vector of the kth species which can be found from the momentum equation. Although the charged species mass conservation does not explicitly include diffusion processes, such are incorporated within the velocity $\boldsymbol{V}^k$ which is the sum of not only the convection but also the diffusion velocities. Following [11], an expression for the charged species velocity in the presence of a magnetic field can be shown to be equal to:

$$\boldsymbol{V}_i^k = \boldsymbol{V}_i + \underbrace{\sum_j s_k \tilde{\mu}_{ij}^k \left(\boldsymbol{E} + \boldsymbol{V} \times \boldsymbol{B}\right)_j}_{\text{drift}} - \underbrace{\sum_j \frac{\tilde{\mu}_{ij}^k}{|q_k| N_k} \frac{\partial P_k}{\partial x_j}}_{\text{diffusion}} \tag{2}$$

where s_k is the sign of the kth species (either -1 for the negatively charged species or +1 otherwise), $\boldsymbol{E}$ is the electric field vector, $\boldsymbol{B}$ is the magnetic field vector, $\boldsymbol{V}$ is the velocity of the plasma bulk (i.e., some average velocity of the mixture composed of the charged and neutral species), N is the number density, and P_k is the partial pressure which can be found from

$$P_k = \begin{cases} N_\mathrm{e} k_\mathrm{B} T_\mathrm{e} & \text{for electron species} \\ N_\mathrm{k} k_\mathrm{B} T & \text{for ions and neutrals species} \end{cases} \tag{3}$$

with T_e the electron temperature, T the translational temperature of the heavy species, and k_B the Boltzmann constant. Also, q_k is the charge of the kth species, which is equal to for instance $+e$ for

Table 1: Modified Park 11-species high-temperature air plasma model.

No.	Reaction[(b)]	Forward Temp.	Backward Temp.	A	n	E [(a)]	Ref.
1	$N_2 + M_1 \rightleftarrows N + N + M_1$	$\sqrt{TT_v}$	T	3.0×10^{22}	-1.6	$113200 \cdot R$	[17]
2	$N_2 + M_2 \rightleftarrows N + N + M_2$	$\sqrt{TT_v}$	T	7.0×10^{21}	-1.6	$113200 \cdot R$	[17]
3	$N_2 + e^- \rightleftarrows N + N + e^-$	$\sqrt{T_e T_v}$	$\sqrt{TT_e}$	3.0×10^{24}	-1.6	$113200 \cdot R$	[17]
4	$O_2 + M_1 \rightleftarrows O + O + M_1$	$\sqrt{TT_v}$	T	1.0×10^{22}	-1.5	$59500 \cdot R$	[17]
5	$O_2 + M_2 \rightleftarrows O + O + M_2$	$\sqrt{TT_v}$	T	2.0×10^{21}	-1.5	$59500 \cdot R$	[17]
6	$NO + M_3 \rightleftarrows N + O + M_3$	$\sqrt{TT_v}$	T	1.1×10^{17}	0.0	$75500 \cdot R$	[17]
7	$NO + M_4 \rightleftarrows N + O + M_4$	$\sqrt{TT_v}$	T	5.0×10^{15}	0.0	$75500 \cdot R$	[17]
8	$NO + O \rightleftarrows N + O_2$	T	T	8.4×10^{12}	0.0	$19400 \cdot R$	[18]
9	$N_2 + O \rightleftarrows NO + N$	T	T	5.7×10^{12}	0.42	$42938 \cdot R$	[19]
10	$N + O \rightleftarrows NO^+ + e^-$	T	$\sqrt{T_e T_v}$	5.3×10^{12}	0.0	$32000 \cdot R$	[20]
11	$O + O \rightleftarrows O_2^+ + e^-$	T	$\sqrt{T_e T_v}$	1.1×10^{13}	0	$81200 \cdot R$	[20]
12	$N + N \rightleftarrows N_2^+ + e^-$	T	$\sqrt{T_e T_v}$	2.0×10^{13}	0	$67700 \cdot R$	[20]
13	$NO^+ + O \rightleftarrows N^+ + O_2$	T	T	1.0×10^{12}	0.5	$77200 \cdot R$	[17]
14	$N^+ + N_2 \rightleftarrows N_2^+ + N$	T	T	1.0×10^{12}	0.5	$12200 \cdot R$	[17]
15	$O_2^+ + N \rightleftarrows N^+ + O_2$	T	T	8.7×10^{13}	0.14	$28600 \cdot R$	[17]
16	$O^+ + NO \rightleftarrows N^+ + O_2$	T	T	1.4×10^{5}	1.90	$26600 \cdot R$	[17]
17	$O_2^+ + N_2 \rightleftarrows N_2^+ + O_2$	T	T	9.9×10^{12}	0.00	$40700 \cdot R$	[17]
18	$O_2^+ + O \rightleftarrows O^+ + O_2$	T	T	4.0×10^{12}	-0.09	$18000 \cdot R$	[17]
19	$NO^+ + N \rightleftarrows O^+ + N_2$	T	T	3.4×10^{13}	-1.08	$12800 \cdot R$	[17]
20	$NO^+ + O_2 \rightleftarrows O_2^+ + NO$	T	T	2.4×10^{13}	0.41	$32600 \cdot R$	[17]
21	$NO^+ + O \rightleftarrows O_2^+ + N$	T	T	7.2×10^{12}	0.29	$48600 \cdot R$	[17]
22	$O^+ + N_2 \rightleftarrows N_2^+ + O$	T	T	9.1×10^{11}	0.36	$22800 \cdot R$	[17]
23	$NO^+ + N \rightleftarrows N_2^+ + O$	T	T	7.2×10^{13}	0.00	$35500 \cdot R$	[17]
24	$O + e^- \rightleftarrows O^+ + e^- + e^-$	T_e	T_e	3.9×10^{33}	-3.78	$158500 \cdot R$	[17]
25	$N + e^- \rightleftarrows N^+ + e^- + e^-$	T_e	T_e	2.5×10^{34}	-3.82	$168600 \cdot R$	[17]
26	$O^+ + e^- \rightarrow O + h\nu$	T_e	–	1.07×10^{11}	-0.52	0	[21]
27	$N^+ + e^- \rightarrow N + h\nu$	T_e	–	1.52×10^{11}	-0.48	0	[21]

[a] The universal gas constant R must be set to 1.9872 cal/K·mol. A has units of $\mathrm{cm}^3 \cdot (\mathrm{mole} \cdot \mathrm{s})^{-1} \cdot \mathrm{K}^{-n}$. E has units of cal/mole.

[b] M_1 = N, O, N^+, O^+, M_2 = N_2, O_2, NO, N_2^+, O_2^+, NO^+, M_3 = N, O, NO, N^+, O^+, M_4 = N_2, O_2, N_2^+, O_2^+, NO^+

the singly-charged positive ions, $-e$ for the electrons, $-2e$ for the doubly-charged negative ions, with e the elementary charge. Also, the tensor mobility $\tilde{\mu}$ corresponds to:

$$\begin{aligned}\tilde{\mu}^k &\equiv \mu_k \begin{bmatrix} 1 & -s_k\mu_k \boldsymbol{B}_3 & s_k\mu_k \boldsymbol{B}_2 \\ s_k\mu_k \boldsymbol{B}_3 & 1 & -s_k\mu_k \boldsymbol{B}_1 \\ -s_k\mu_k \boldsymbol{B}_2 & s_k\mu_k \boldsymbol{B}_1 & 1 \end{bmatrix}^{-1} \\ &= \frac{\mu_k}{1+\mu_k^2|\boldsymbol{B}|^2} \begin{bmatrix} 1+\mu_k^2\boldsymbol{B}_1^2 & \mu_k^2\boldsymbol{B}_1\boldsymbol{B}_2 + s_k\mu_k\boldsymbol{B}_3 & \mu_k^2\boldsymbol{B}_1\boldsymbol{B}_3 - s_k\mu_k\boldsymbol{B}_2 \\ \mu_k^2\boldsymbol{B}_1\boldsymbol{B}_2 - s_k\mu_k\boldsymbol{B}_3 & 1+\mu_k^2\boldsymbol{B}_2^2 & \mu_k^2\boldsymbol{B}_2\boldsymbol{B}_3 + s_k\mu_k\boldsymbol{B}_1 \\ \mu_k^2\boldsymbol{B}_1\boldsymbol{B}_3 + s_k\mu_k\boldsymbol{B}_2 & \mu_k^2\boldsymbol{B}_2\boldsymbol{B}_3 - s_k\mu_k\boldsymbol{B}_1 & 1+\mu_k^2\boldsymbol{B}_3^2 \end{bmatrix}\end{aligned} \tag{4}$$

Table 2: Ion and electron mobilities in dry air.[a]

Species	Mobility μ, $\mathrm{m^2 \cdot V^{-1} \cdot s^{-1}}$	Reference
N_2^+	$N^{-1} \cdot \min\left(0.75 \cdot 10^{23} \cdot T^{-0.5},\ 2.03 \cdot 10^{12} \cdot (E^\star)^{-0.5}\right)$	[22]
O_2^+	$N^{-1} \cdot \min\left(1.18 \cdot 10^{23} \cdot T^{-0.5},\ 3.61 \cdot 10^{12} \cdot (E^\star)^{-0.5}\right)$	[22]
N^+	$N^{-1} \cdot \min\left(1.05 \cdot 10^{23} \cdot T^{-0.5},\ 2.84 \cdot 10^{12} \cdot (E^\star)^{-0.5}\right)$	[22, 23]
O^+	$N^{-1} \cdot \min\left(1.65 \cdot 10^{23} \cdot T^{-0.5},\ 5.05 \cdot 10^{12} \cdot (E^\star)^{-0.5}\right)$	[22, 23]
e^-	$\dfrac{1}{\dfrac{N_\mathrm{n}}{3.74 \cdot 10^{19} \cdot \exp\left(33.5/\sqrt{\ln T_\mathrm{e}}\right)} + \dfrac{N_\mathrm{i}}{1.061 \cdot 10^{16} \cdot T_\mathrm{e}^{1.5}}}$	[13],[24, pp. 180-181][b]

[a] Notation and units: T_e is the electron temperature in Kelvin; T is the heavy particle translational temperature in Kelvin; N is the total number density of the plasma in $1/\mathrm{m^3}$; N_i is the sum of the positive ion number densities in $1/\mathrm{m^3}$; N_n is the sum of the neutral species number densities in $1/\mathrm{m^3}$; N_i is the sum of the ion species number densities in $1/\mathrm{m^3}$; $E^\star$ is the reduced effective electric field ($E^\star \equiv |\boldsymbol{E}|/N$) in units of $\mathrm{V \cdot m^2}$.

[b] The electron mobility includes both electron-neutral and electron-ion collisions.

with μ the mobility which can be found for the ions and electrons in Table 2 At the solid surfaces, the gradient of the mass fraction of the neutral species can generally be set to zero when there is no surface catalysis. In contrast, the charged species can not be given a non-catalytic boundary condition. Rather, a fraction of the ions that travel towards the surface ions release an electron (secondary electron emission) while the rest recombine with the incoming electrons at the surface. Both effects can be represented through the following boundary condition for the charged species as outlined in Ref. [14]:

$$\frac{\partial}{\partial \chi} N_+ \boldsymbol{V}_\chi^+ = 0 \ \text{ and } \ N_- = 0 \ \text{ and } \ N_\mathrm{e} = \frac{\gamma}{\mu_\mathrm{e}} \sum_{k=1}^{n_\mathrm{s}} N_k \mu_k \beta_k^+ \ \text{ for } \boldsymbol{E}_\chi < 0 \tag{5}$$

$$N_+ = 0 \quad \text{and} \quad \frac{\partial}{\partial \chi} N_- \boldsymbol{V}_\chi^- = 0 \quad \text{and} \quad \frac{\partial}{\partial \chi} N_\mathrm{e} \boldsymbol{V}_\chi^\mathrm{e} = 0 \quad \text{otherwise} \tag{6}$$

where the subscripts "+" and "-" refer to the positive and negative ions respectively, and the subscript "e" refers to the electrons, and β_k^+ is equal to 1 should the kth species be a positive ion and to zero otherwise. Also, n_s is the number of species, χ is a coordinate perpendicular to the surface and pointing towards the fluid, and γ is the secondary emission coefficient which is not well known (because it depends on surface temperature, composition, and roughness) and is here varied between 0.1 and 5.

In the above, the magnetic field is specified and it is assumed that the induced magnetic field is small compared to the externally applied magnetic field (from a magnet installed on board the vehicle). Because we can assume electrostatics, the electric field can be found from a potential equation based on Gauss's law as follows:

$$\nabla^2 \phi = -\frac{\rho_\mathrm{c}}{\epsilon_0} \tag{7}$$

with ϕ the electric field potential, ρ_c the net charge density, ϵ_0 the permittivity of free space. Knowing ϕ we can find the electric field as $\boldsymbol{E} = -\boldsymbol{\nabla}\phi$.

B. Multispecies Navier-Stokes Equations

For the neutral species, the mass conservation equation includes convection and diffusion terms as follows:

$$\frac{\partial \rho_k}{\partial t} + \sum_{i=1}^{3} \frac{\partial}{\partial x_i} \boldsymbol{V}_i \rho_k - \sum_{i=1}^{3} \frac{\partial}{\partial x_i} \nu_k \frac{\partial w_k}{\partial x_i} = W_k \tag{8}$$

where w_k is the mass fraction of the kth species and ν_k is the diffusion coefficient which is found from the Lennard-Jones potentials [25]. The momentum equation for the bulk of the plasma includes source terms to account for the electromagnetic body forces:

$$\frac{\partial}{\partial t} \rho \boldsymbol{V}_i + \sum_{j=1}^{3} \frac{\partial}{\partial x_j} \rho \boldsymbol{V}_j \boldsymbol{V}_i = -\frac{\partial P}{\partial x_i} + \sum_{j=1}^{3} \frac{\partial \tau_{ji}}{\partial x_j} + \rho_c \boldsymbol{E}_i + (\boldsymbol{J} \times \boldsymbol{B})_i \tag{9}$$

with P being the sum of all partial pressures including the electron pressure and $\boldsymbol{J}$ being the current density equal to $\boldsymbol{J} \equiv \sum_k N_k \boldsymbol{V}^k q_k$. Also, τ_{ji} is the Navier stress tensor in which the viscosity of the mixture is found from Wilke's mixing rule.

C. Energy Transport Equations

The electron temperature T_e needed to find some chemical reaction rates and to find the electron partial pressure P_e is determined from the following electron energy transport equation [16]:

$$\frac{\partial}{\partial t} \rho_e e_e + \sum_{j=1}^{3} \frac{\partial}{\partial x_j} \rho_e \boldsymbol{V}_j^e h_e = W_e e_e + \boldsymbol{E} \cdot \boldsymbol{J}_e - Q_{en} - Q_{ei} \tag{10}$$

where e_e and h_e are the electron specific energy and specific enthalpy equal to $\frac{3}{2}\frac{k_B}{m_e}T_e$ and to $\frac{5}{2}\frac{k_B}{m_e}T_e$, respectively. Also, Q_{en} is the energy exchange of the electrons with the neutrals and can be shown to correspond to [26]:

$$Q_{en} = \frac{3 N_e k_B (T_e - T)|q_e|\zeta_e}{2 m_e \mu_e} \tag{11}$$

with m_e is the electron mass. Also Q_{ei} is the heat needed for electron-impact ionization, and $\boldsymbol{J}_e$ is the electron current equal to $q_e N_e \boldsymbol{V}^e$. In the latter, although the electron thermal diffusion $\kappa_e \partial_x T_e$ does not appear explicitly, it is incorporated within the convection of the electron enthalpy because $\boldsymbol{V}_j^e$ includes electron pressure gradients. Also, the electron energy loss function ζ_e is as specified in [16].

The translation temperature T is determined from the total energy equation:

$$\begin{aligned} &\frac{\partial}{\partial t} \rho e_t + \sum_{j=1}^{3} \frac{\partial}{\partial x_j} \boldsymbol{V}_j (\rho e_t + P) - \sum_{j=1}^{3} \frac{\partial}{\partial x_j} \left(\sum_{k=1}^{n_s} \beta_k^n \nu_k (h_k + h_k^\circ) \frac{\partial w_k}{\partial x_j} \right) \\ &+ \sum_{j=1}^{3} \sum_{k=1}^{n_s} \frac{\partial}{\partial x_j} \left(\beta_k^c \rho_k (\boldsymbol{V}_j^k - \boldsymbol{V}_j)(h_k + h_k^\circ) \right) - \sum_{i=1}^{3} \frac{\partial}{\partial x_i} \left(\kappa \frac{\partial T}{\partial x_i} \right) = \sum_{i=1}^{3} \sum_{j=1}^{3} \frac{\partial}{\partial x_j} \tau_{ji} \boldsymbol{V}_i + \boldsymbol{E} \cdot \boldsymbol{J} \end{aligned} \tag{12}$$

where β_k^{n} is equal to 1 should species k be neutral and to 0 otherwise and β_k^{c} is equal to 1 should species k be charged and to 0 otherwise. Also, the thermal conductivity κ is found from the Mason and Saxena relationship and e_{t} corresponds to the total specific energy:

$$e_{\mathrm{t}} \equiv \sum_{k=1}^{n_{\mathrm{s}}} w_k (e_k + h_k^{\circ}) + \frac{1}{2}|\boldsymbol{V}|^2 \tag{13}$$

In the latter, h_k° stands for the heat of formation while the sum $(h_k + h_k^{\circ})$ represents the enthalpy of the kth species including calorically-imperfect effects as well as the heat of formation and is obtained from the NASA Glenn high temperature enthalpy polynomials [27].

III. Numerical Methods

The convection derivatives are discretized using the Roe scheme turned second-order accurate through the Van-Leer TVD limiter. The accuracy of the discretization stencil is improved through a positivity-preserving filter applied to the flux at the interface [28, 29]. Such filter prevents the flux from giving negative mass fractions or negative temperatures and also improves considerably the stability of the integration process. Carbuncles and other non-physical phenomena are prevented through eigenvalue conditioning with a pressure gradient sensor as outlined in [30]. Such eigenvalue conditioning does not affect the capability of the Roe scheme to capture viscous layers with high resolution.

In Refs. [13, 14], it was shown that the drift-diffusion equations (presented above within the Physical Model section) could be converged with time steps several orders of magnitude larger than usual through a recast of the system. The recast consists of obtaining the electric field potential from Ohm's law rather than from Gauss's law, of modifying the ion transport equation such that Gauss's law is satisfied, and of rewriting the electron transport equation in ambipolar form. The reason why the recast system is more computationally efficient than the standard system is twofold: (i) the recast system avoids error-amplifying terms that are present within the Gauss-based potential equation and that prevent high time steps to be used, and (ii) the recast system exhibits a higher resolution of the converged solution because of the ambipolar form reducing the magnitude of the terms to be discretized and thus leading to less numerical error. We here apply this recast in order to relieve the stiffness associated with the standard set of equations to obtain faster convergence. This permits the use of much finer meshes and help reduce numerical error. It is emphasized that this recast of the drift-diffusion does not take shortcuts and add/remove any physics outlined in Section II.. Rather, the recast is strictly a convergence acceleration method as it does ensure that all equations listed in Section II. are converged as the mesh is refined.

The mass, momentum, and energy transport equations are iterated through a block diagonally-dominant alternate-direction-implicit (block DDADI) method [31] which is chosen because of its good high frequency damping characteristics. The electric field potential equation is iterated through a mix of successive over relaxation and iteration modified approximate factorization [32] algorithms.

IV. Problem Setup

To investigate the effect of plasma sheaths on MHD induced forces and heating, a two-dimensional channel flow is simulated whose schematic is shown in Fig.1(b). The inflow properties of the channel flow correspond to a Mach number of 4 and are obtained by probing a location downstream of a bow shock formed over a blunt-body whose schematic is shown in Fig.1(a). For both the blunt-body and channel flow simulations, a no-slip condition is used at the surface/walls and the wall-temperature is fixed to 3000 K. After obtaining a steady-state solution over the blunt-body, the flow speed, pressure, temperature and molar fractions of the chemical species from the probed location are used as the inflow properties for the channel flow simulation. In the channel flow simulation, two electrodes sit flush with the wall surface and the rest of the walls are dielectrics. The effect of magnetic fields and secondary electron emission coefficient on the flowfield is investigated by applying different values of magnetic fields in the spanwise direction (z-direction).

V. Preliminary Results

The 2D channel flow simulations are run with different magnetic fields (B_z) ranging from 0.2 - 0.6 T. Two secondary electron emission coefficient values (γ = 0.1 and 1) are tested for each magnetic field. The resulting MHD induced forces and heat in the domain are tabulated in Table.3.

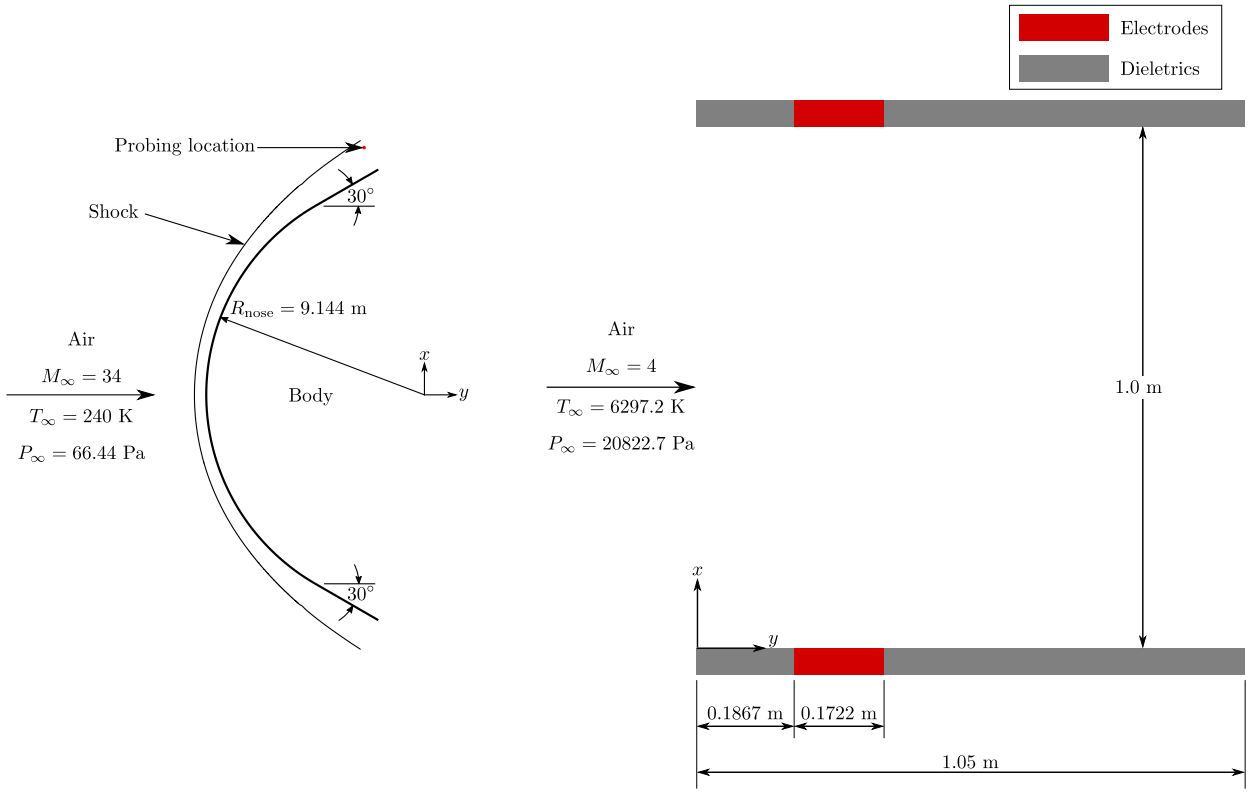

(a) Schematic of blunt body **(b)** Schematic of channel

Fig. 1: Problem setup for the simulations in the present study

Table 3: Effect of secondary electron emission coefficient on body forces.

B_z, T	γ	$F_{\text{emfield},x}$, N/m	$F_{\text{emfield},y}$, N/m	Joule heating, W/m
0.2	0.1	-16600	-2640	4.40×10^7
	1	-24350	-3500	2.69×10^7
0.4	0.1	-94700	-13300	6.80×10^7
	1	-113600	-13400	5.03×10^7
0.6	0.1	choking	choking	choking
	1	choking	choking	choking

A. Effect of the Secondary Electron Emission Coefficient

One parameter that affects significantly the body force is the secondary electron emission coefficient, γ. As can be seen from the results shown in Table 3, a change of γ from 0.1 to 1.0 leads to the body force increasing by a very appreciable 20-30%. For a low γ, the cathode sheath opposes considerable resistance to current because the current within the sheath is mostly ionic (low conductivity) and not electronic (higher conductivity). As γ is increased, the cathode sheath becomes more highly populated with electrons and its resistance to current flow consequently decreases. This sensitivity of the body force on the secondary electron emission coefficient shows the importance of including the sheath within the simulations of MHD processes. This further shows the importance of determining the precise value for the secondary electron emission coefficient. We here vary it between 0.1 and 1.0 because it is not well known and depends on various parameters such as the surface composition, the amount of oxidation, the surface temperature, etc. Experiments are needed to pinpoint the value of γ accurately in order to reduce the error uncertainty coming from γ on the MHD system performance.

B. Effect of the Applied Magnetic Field

In theory, we would expect a twofold increase of the magnetic field to lead to a fourfold increase in the body forces. This is because the Lorentz force scales with the product of the current density and the magnetic field, and the current density scales with the magnetic field. Indeed, because the electrodes are short circuited, there is no electric field perpendicular to the flow and the current density flowing between the electrodes will scale with the magnetic field, following the Faraday EMF principle.

However, the numerical results don't follow the theory perfectly. For a twofold increase in the magnetic field, we obtain rather a five to six-fold increase in the body forces, rather than the predicted fourfold increase (see results in Table 3). Although more analysis needs to be done to confirm this, it seems that the reason for this anomaly comes from the plasma sheath. At a low magnetic field, the plasma sheath blocks a larger fraction of the current than at a higher magnetic field. Thus, as the magnetic field is lowered two separate physical phenomena contribute to a decrease in the current and, thus, of the Lorentz force: (i) the current decreases proportionally with the magnetic field following the Faraday EMF, (ii) the current is further reduced by the plasma sheath resistance.

For applied magnetic fields greater than 0.3 T, substantial deceleration of the flow is observed,

resulting in unsteadiness and waves propagating obliquely to the walls as seen in Figures 2-5. Such oblique waves were observed previously in [33] within a MHD device and were attributed to a Hall parameter effect. When the Hall parameter exceeds 1 (as is the case here at a magnetic field exceeding 0.3 Tesla), the current does not flow linearly between the electrodes but flows at an angle. This leads in some cases to unsteady oblique waves forming. A better analysis of the origin of these oblique waves and their impact on the performance of the MHD system will be outlined in the final paper.

For magnetic fields of 0.5 T and greater no meaningful results could be obtained because the Lorentz force was strong enough to lead to the average Mach number at the exit of the channel falling below 1. Then, the flow chokes and a strong normal shockwave propagates upstream until it reaches the supersonic inflow boundary on the left of the channel domain. Such a situation has been denoted as "choking" in Table 3.

Acknowledgment

This study has been sponsored by a NASA NIAC Phase 1 award.

References

[1] Fujino, T., Yoshino, T., and Ishikawa, M., "Numerical analysis of reentry trajectory coupled with magnetohydrodynamics flow control," *Journal of Spacecraft and Rockets*, Vol. 45, No. 5, 2008, pp. 911–920.

[2] Bityurin, V., Bocharov, A., Baranov, D., Popov, N., Alferov, V., and Tikhonov, V., "Progress in MHD parachute concept study," *49th AIAA Aerospace Sciences Meeting including the New Horizons Forum and Aerospace Exposition*, 2011, p. 902.

[3] Gildfind, D. E., Smith, D., Jacobs, P. A., Kelly, R., Lefevre, A., and McIntyre, T. J., "Expansion Tube Test Flow Design for Magnetohydrodynamic Aerobraking," *AIAA Journal*, Vol. 59, No. 4, 2021, pp. 1328–1341.

[4] Macheret, S., Shneider, M., Candler, G., Moses, R., and Kline, J., "Magnetohydrodynamic power generation for planetary entry vehicles," *35th AIAA Plasmadynamics and Lasers Conference*, 2004, p. 2560.

[5] Wan, T., Candler, G. V., Macheret, S. O., and Shneider, M. N., "Three-Dimensional Simulation of the Electric Field and Magnetohydrodynamic Power Generation During Reentry," *AIAA Journal*, Vol. 47, No. 6, 2009, pp. 1327.

[6] Bityurin, V., Bocharov, A., Baranov, D., Bychkov, S., and Podmazov, A., "Power extraction experiment with a surface MHD generator in hypersonic airflow," *38th AIAA Plasmadynamics and Lasers Conference In conjunction with the 16th International Conference on MHD Energy Conversion*, 2007, p. 3882.

[7] Meyer, R. C., "On reducing aerodynamic heat-transfer rates by magnetohydrodynamic techniques," *Journal of the Aerospace Sciences*, Vol. 25, No. 9, 1958, pp. 561–566.

[8] Cristofolini, A., Borghi, C. A., Neretti, G., Schettino, A., Trifoni, E., Battista, F., Passaro, A., and Baccarella, D., "Experimental investigations on the magneto-hydro-dynamic interaction around a blunt body in a hypersonic unseeded air flow," *Journal of Applied Physics*, Vol. 112, No. 9, 2012, pp. 093304.

[9] Li, K., Liu, J., and Liu, W., "Performance Analysis and Enhancement of Magnetohydrodynamic Heat Shield System For Hypersonic Vehicles," *21st AIAA International Space Planes and Hypersonics Technologies Conference*, 2017, p. 2214.

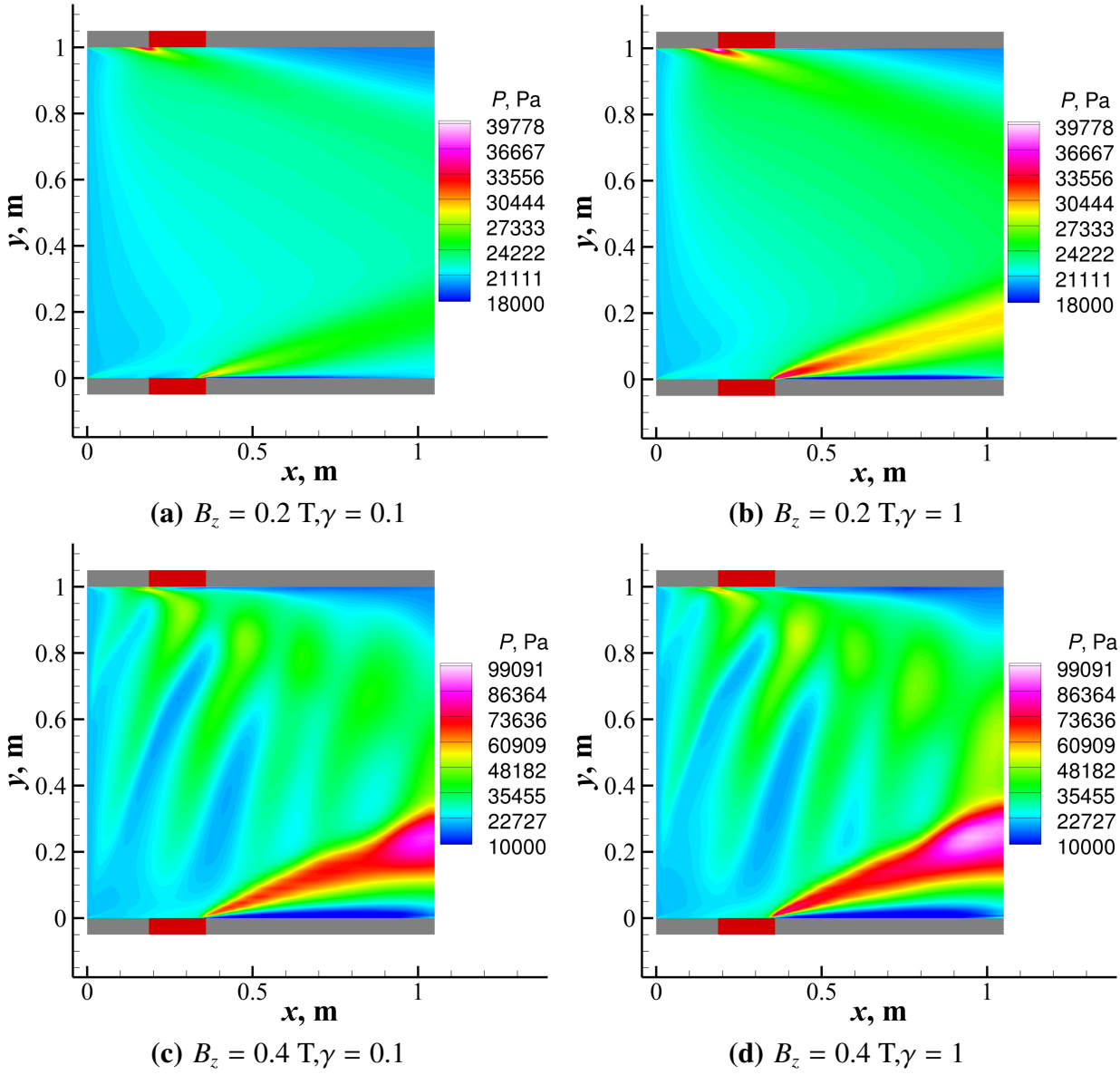

(a) $B_z = 0.2$ T,$\gamma = 0.1$ **(b)** $B_z = 0.2$ T,$\gamma = 1$

(c) $B_z = 0.4$ T,$\gamma = 0.1$ **(d)** $B_z = 0.4$ T,$\gamma = 1$

Fig. 2: Effect of varying magnetic field and secondary electron emission on pressure.

[10] Kkn, A. and Reddy, K., "Measurement of heat-flux for magneto-aerodynamic interaction studies in a hypersonic flow," *47th AIAA Plasmadynamics and Lasers Conference*, 2016, p. 4143.

[11] Parent, B., Shneider, M. N., and Macheret, S. O., "Generalized Ohm's Law and Potential Equation in Computational Weakly-Ionized Plasmadynamics," *Journal of Computational Physics*, Vol. 230, No. 4, 2011, pp. 1439–1453.

[12] Parent, B., Macheret, S. O., and Shneider, M. N., "Ambipolar Diffusion and Drift in Computational Weakly-Ionized Plasmadynamics," *Journal of Computational Physics*, Vol. 230, No. 22, 2011, pp. 8010–8027.

[13] Parent, B., Shneider, M. N., and Macheret, S. O., "Sheath Governing Equations in Computational Weakly-Ionized Plasmadynamics," *Journal of Computational Physics*, Vol. 232, No. 1, 2013, pp. 234–251.

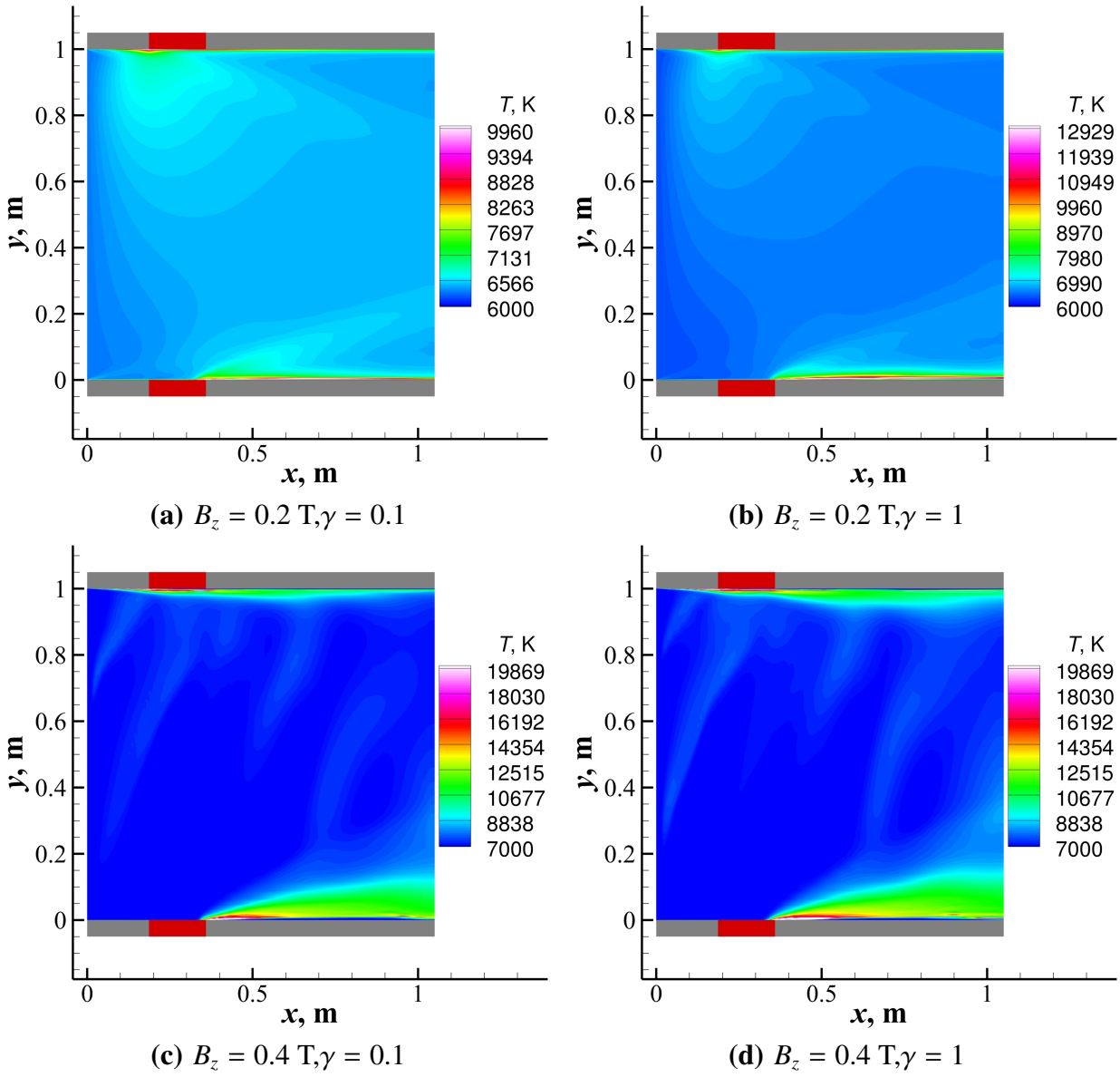

(a) $B_z = 0.2$ T,$\gamma = 0.1$ **(b)** $B_z = 0.2$ T,$\gamma = 1$

(c) $B_z = 0.4$ T,$\gamma = 0.1$ **(d)** $B_z = 0.4$ T,$\gamma = 1$

Fig. 3: Effect of varying magnetic field and secondary electron emission on temperature.

[14] Parent, B., Macheret, S. O., and Shneider, M. N., "Electron and Ion Transport Equations in Computational Weakly-Ionized Plasmadynamics," *Journal of Computational Physics*, Vol. 259, 2014, pp. 51–69.

[15] Parent, B., Macheret, S. O., and Shneider, M. N., "Modeling weakly-ionized plasmas in magnetic field: A new computationally-efficient approach," *Journal of Computational Physics*, Vol. 300, 2015, pp. 779–799.

[16] Parent, B., "Electron Heating and Cooling in Hypersonic Flows," *Physics of Fluids*, Vol. 33, No. 4, 2021, pp. 046105.

[17] Park, C., *Nonequilibrium Hypersonic Aerothermodynamics*, Wiley, New-York, 1990.

[18] Bose, D. and Candler, G. V., "Thermal rate constants of the O2+N→NO+O reaction based on the A2 and A4 potential-energy surfaces," *The Journal of Chemical Physics*, Vol. 107, No. 16, 1997, pp. 6136–6145.

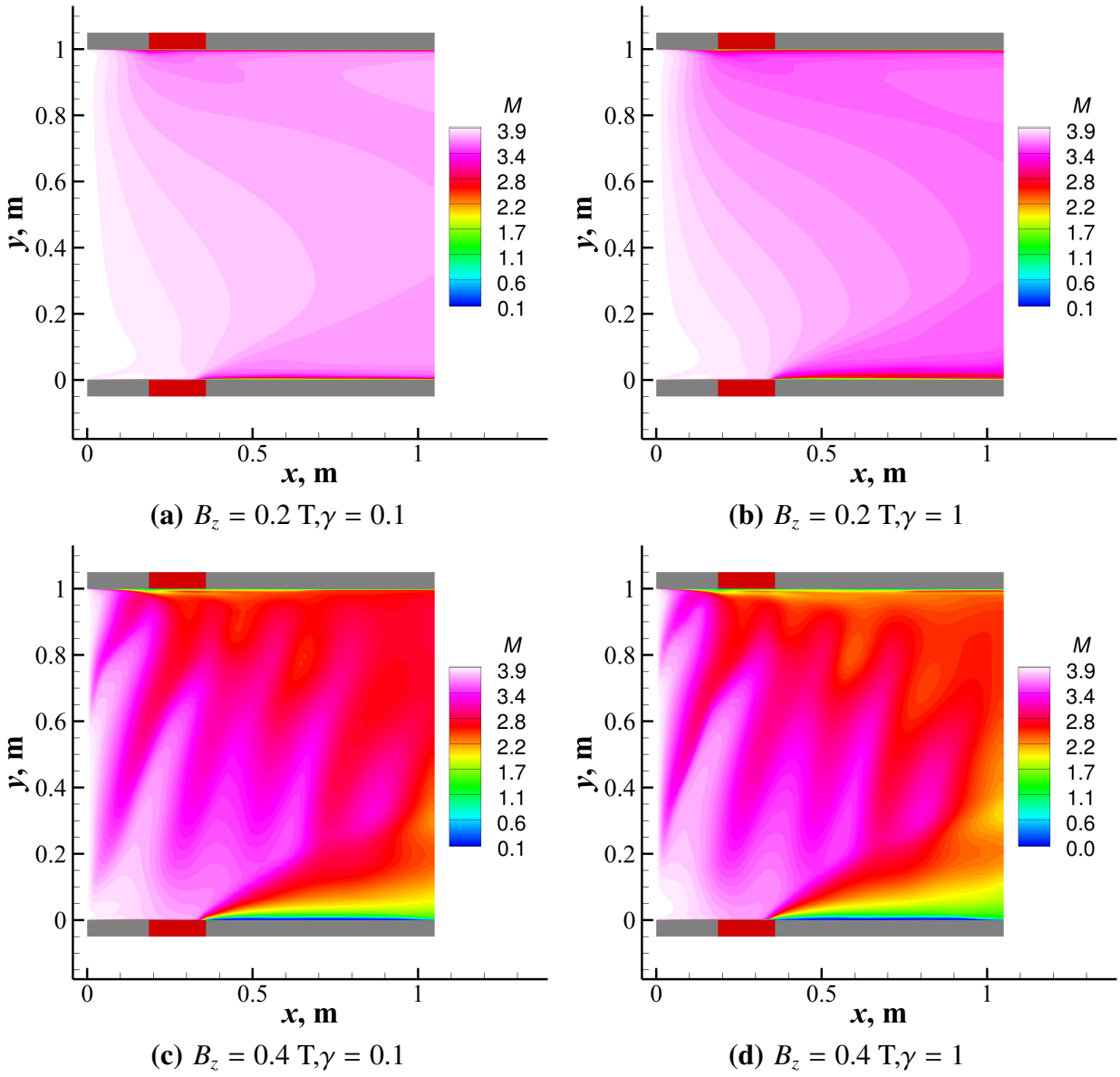

(a) $B_z = 0.2$ T,$\gamma = 0.1$ **(b)** $B_z = 0.2$ T,$\gamma = 1$

(c) $B_z = 0.4$ T,$\gamma = 0.1$ **(d)** $B_z = 0.4$ T,$\gamma = 1$

Fig. 4: Effect of varying magnetic field and secondary electron emission on Mach number.

[19] Bose, D. and Candler, G. V., "Thermal rate constants of the N2+O→NO+N reaction using ab initio 3A and 3A potential energy surfaces," *The Journal of Chemical Physics*, Vol. 104, No. 8, 1996, pp. 2825–2833.

[20] Boyd, I. D., "Modeling of associative ionization reactions in hypersonic rarefied flows," *Physics of Fluids*, Vol. 19, No. 9, 2007, pp. 096102.

[21] Park, C., "Review of Chemical-Kinetic Problems of Future NASA Missions, I: Earth Entries," *Journal of Thermophysics and Heat Transfer*, Vol. 7, No. 3, 1993, pp. 385–398.

[22] Sinnott, G., Golden, D. E., and Varney, R. N., "Positive-Ion Mobilities in Dry Air," *Physical Review*, Vol. 170, No. 1, 1968, pp. 272–275.

[23] Ungethüm, E., "The mobilities of small ions in the atmosphere and their relationship," *Journal of Aerosol Science*, Vol. 5, No. 1, 1974, pp. 25–37.

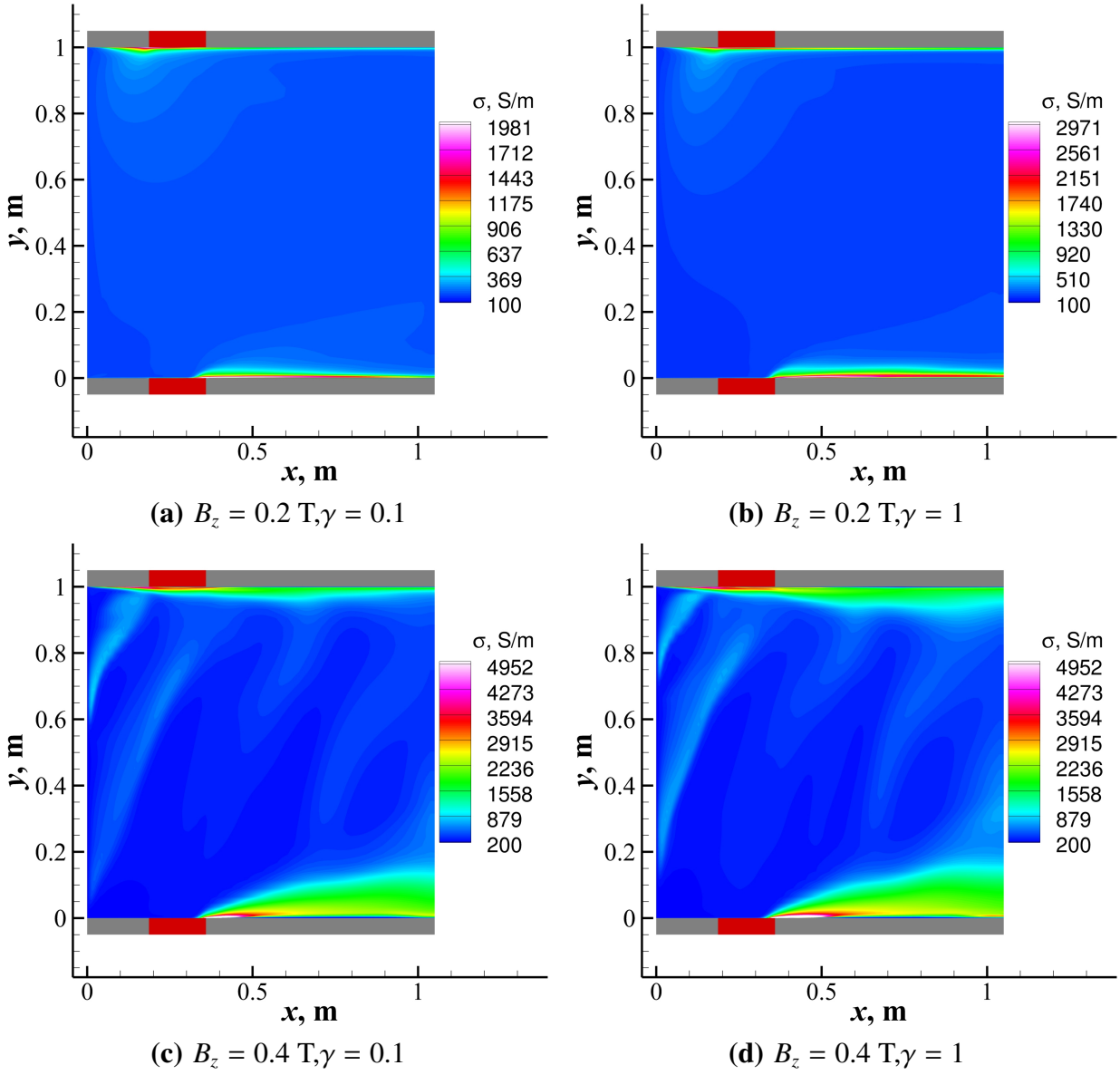

Fig. 5: Effect of varying magnetic field and secondary electron emission on electrical conductivity.

[24] Chen, F. F., *Introduction to Plasma Physics and Controlled Fusion Volume 1: Plasma Physics*, Plenum Press, New York, NY, 1984.

[25] Svehla, R. A., "Estimated Viscosities and Thermal Conductivities of Gases at High Temperature," *NASA TR R-132*, 1962.

[26] Raizer, Y. P., *Gas Discharge Physics*, Springer-Verlag, Berlin, Germany, 1991.

[27] McBride, B. J., Z. M. J. and Gordon, S., "NASA Glenn Coefficients for Calculating Thermodynamic Properties of Individual Species," *TP 211556, NASA*, 2002.

[28] Parent, B., "Positivity-preserving flux difference splitting schemes," *Journal of Computational Physics*, Vol. 243, 2013, pp. 194–209.

[29] Parent, B., "Making a Flux Positivity-Preserving: A General Purpose Filter for the Euler Equations," *AIAA Paper 2019-0906*, 2019, AIAA Scitech Conference, San Diego, CA.

[30] Parent, B., "Positivity-Preserving Dual Time Stepping Schemes for Gas Dynamics," *Journal of Computational Physics*, Vol. 361, 2018, pp. 391–411.

[31] Bardina, J. E. and Lombard, C. K., "Three Dimensional Hypersonic Flow Simulations with the CSCM Implicit Upwind Navier-Stokes Method," *AIAA Paper 87-1114*, 1987, Proceedings of the 8th AIAA Computational Fluid Dynamics Conference.

[32] MacCormack, R. W., "Iterative Modified Approximate Factorization," *Computers and Fluids*, Vol. 30, No. 8, 2001, pp. 917–925.

[33] Parent, B., Macheret, S., Shneider, M., and Harada, N., "Numerical Study of an Electron-Beam-Confined Faraday Accelerator," *Journal of Propulsion and Power*, Vol. 23, No. 5, 2007, pp. 1023–1032.